Chapter 9
FRF Error Mitigation Methods for time Waveform Replication

Keaton Coletti, Steven Carter, and Ryan Schultz

Abstract Time waveform replication (TWR) must be performed carefully to avoid errors in the output waveform. A key source of error in multi-input, multi-output TWR is error in the measured frequency response functions (FRFs). If an inverse Fast Fourier Transform (IFFT) is performed on the measured FRFs, the error appears as non-causal growth at the end of the resulting signals. When non-causal FRFs are applied to TWR control, significant errors between the target and system responses occur: in particular, the system responds to transient events such as shocks before prescribed in the target response. This paper shows that non-causal effects due to noise are distinct from effects due to finite bandwidth in measured FRFs. Using a TWR framework that does not require any time-domain windowing, several FRF error mitigation techniques are explored. The techniques are compared in a time waveform replication simulation featuring three inputs and eight outputs.

Keywords time-waveform replication · multi-input multi-output · FRF causality · transient control

Introduction

Time waveform replication (TWR) is the process of replicating a time-domain waveform in the output of a dynamic system. In structural dynamics, performing TWR in a laboratory setting is critical to the qualification of, *e.g.*, automotive and aeronatical components and assemblies. These may be subjected to complicated loading environments during service, including combinations of random vibration, harmonic vibration, transient vibration, and shock. Multi-input, multi-output (MIMO) testing is growing in popularity for TWR testing because it enables better replication of the entire structure's field response in the laboratory than with single-axis testing. MIMO TWR can be performed using electrodynamic shakers or on a six-degree-of-freedom shaker table. Whether in an open- or closed-loop, MIMO TWR control typically involves a variant of Fourier deconvolution, wherein inputs are solved for in the frequency domain by posing the time-domain convolution with impulse response functions (IRFs) as independent multiplication problems with the frequency response functions (FRFs).

To perform TWR, accurate estimates of the system frequency response functions are essential. Extensive prior works have investigated the best practices for FRF estimation [1–3], with some focusing specifically on the TWR problem [4]. However, apparently sparsely addressed in the context of MIMO TWR are the specific "causality" issues that occur during time waveform replication. In some configurations, the standard least-squares Fourier deconvolution approach yields inputs corresponding to events in the output specification at the wrong time. For instance, if a shock event occurs at 2 seconds, Fourier deconvolution may yield high input levels at 1.9 seconds, resulting in a "pre-echo" in the output waveform, wherein the system responds to the specification before it occurs. Such causality issues are the subject of this paper. Causal system identification has been researched in some fields of electrical engineering [5–7], but many of the approaches are not applicable to TWR because they involve continuous or infinite transfer functions, or they allow extrapolation outside of the test bandwidth [8–10]. In this paper, the system FRFs are assumed to be experimentally measured and are allowed to be modified. FRF estimation for TWR is not addressed in this paper.

Keaton Coletti · Steven Carter · Ryan Schultz
Sandia National Laboratories, Albuquerque, NM 87185
e-mail: keaton.coletti@uga.edu; kpcolet@sandia.gov; spcarte@sandia.gov; rschult@sandia.gov

Brandon Dilworth et al. (eds.), *Topics in Modal Analysis & Parameter Identification II, Vol. 10*, Conference Proceedings of the Society for Experimental Mechanics Series, https://doi.org/10.13052/97887-438-0155-9_9

TWR Background

The goal of TWR is to produce a system output, $\mathbf{y}(t_n)$, $n = 1, 2, \ldots, N$, that matches a specified output, $\mathbf{y}_{\text{spec}}(t_n)$. The sample rate is given by $t_{n+1} - t_n = 1/f_s$, and $\mathbf{y}, \mathbf{y}_{\text{spec}} \in \mathbb{R}^{N_o}$. N_o is the number of output channels in the specification. The system is described by a discrete representation of the frequency response matrix (FRM), $\widehat{\mathbf{H}}(\omega_k) \in \mathbb{C}^{N_o \times N_i}$. N_i is the number of input (excitation) locations used to generate the output waveform.

Denote the discrete Fourier Transform by $\mathcal{F}$ and the inverse discrete Fourier Transform by $\mathcal{F}^{-1}$. These are typically computed using the Fast Fourier Transform (FFT) algorithm. Define $\widehat{\mathbf{y}}(\omega_k)$, $k = 1, 2, \ldots, K$ as $\mathcal{F}(\mathbf{y}(t_n))$ TWR is usually performed by solving a series of frequency-domain (FFT-transformed) least-squares problems,

$$\widehat{\mathbf{x}}(\omega_k) = \arg\min_{\mathbf{z}} \left|\left| \hat{\mathbf{y}}_{\text{spec}}(\omega_k) - \hat{\mathbf{H}}(\omega_k)\,\mathbf{z} \right|\right|_2, \tag{1}$$

where $\circ^H$ denotes the Hermitian operator, and $\hat{\mathbf{x}}$ is the frequency-domain system input. Similar formulations exist for regularized versions of the inverse problem, which consider the size of $\widehat{\mathbf{x}}$ in addition to the residuals. The time-domain and frequency-domain problem forms are related by the discrete form of the circular convolution theorem,

$$\mathbf{y}(t_n) = \mathcal{F}^{-1}\left(\mathcal{F}(\mathbf{H}(t_n))\,\mathcal{F}(\mathbf{x}(t_n))\right) = \sum_{j=0}^{N-1} \mathbf{H}_p(t_j)\,\mathbf{x}_p(t_{n-j}). \tag{2}$$

Here $\circ_p$ denotes the N-periodic infinite extension of a series. Hence, the frequency-domain TWR problem solves the question: “what infinitely repeating input will generate the infinitely repeating output specification,” which has a different solution than if the system starts and ends at rest. To avoid this “convolution wraparound error,” the beginning and end of the specification are zero-padded [11].

Long specifications that include many output channels can result in high or prohibitive computational cost to compute the FFT. The constant overlap add method (COLA) is often used for long TWR problems. COLA involves windowing the specification, solving for each window, and concatenating the inputs into a single sequence. Though COLA can reduce memory usage, the windowing and stitching process can introduce additional leakage errors. Hence, this paper uses a single-frame TWR framework. FFTs of the specification and IFFTs of the solved input can be computed for groups of channels in serial, and $\mathbf{x}(\omega_k)$ can be computed in groups in serial. The group size is determined by the system memory, and each group can be computed in parallel. The only condition is that the system memory should be (as a rough rule of thumb) at least eight times the size of a single channel's record. On a computer with 64 GB of memory, this is 10^9 double-precision values, or just under 3 hours of data sampled at 100 kHz. Practical applications rarely require longer data records than this.

Though the impulse response function (IRF) is the inverse Fourier Tranform of the frequency response function (FRF), the IFFT of the discrete FRF is not a discrete representation of the IRF. First, note that truncation in the time-domain is discretization in the frequency domain, and discretization in the frequency domain is truncation in the time domain. Fig. 1 shows FRF windowing (truncation) in the frequency domain, and Fig. 2 shows the same windowing in the time domain. In the top row, the operations are multiplication and truncation, and in the bottom row, the operations are convolution and downsampling. FRF truncation results in an apparent “non-causal” ring at the end of the IFFT of the FRF. The IFFT of the FRF is a finite discrete representation of the bandpass-filtered IRF, which cannot go from zero to nonzero instantly.

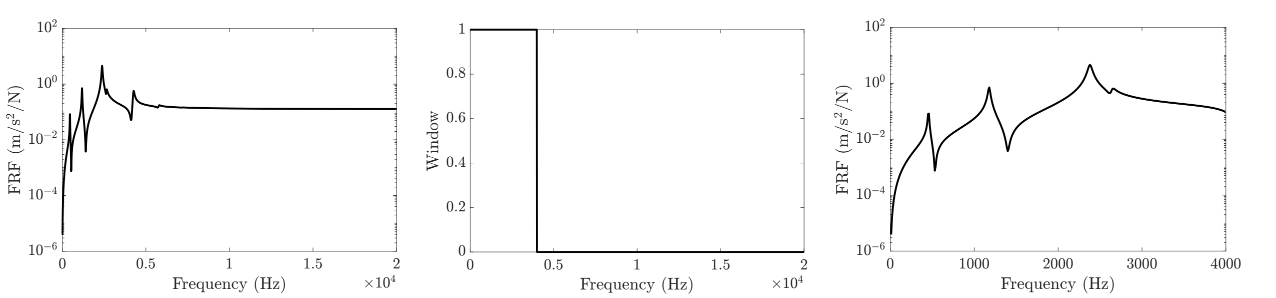

(a) (b) (c)

Fig. 1 Visualization of the effects of frequency truncation on the FRF in the frequency domain. Subfigure (a) is multiplied by (b) and truncated to yield (c).

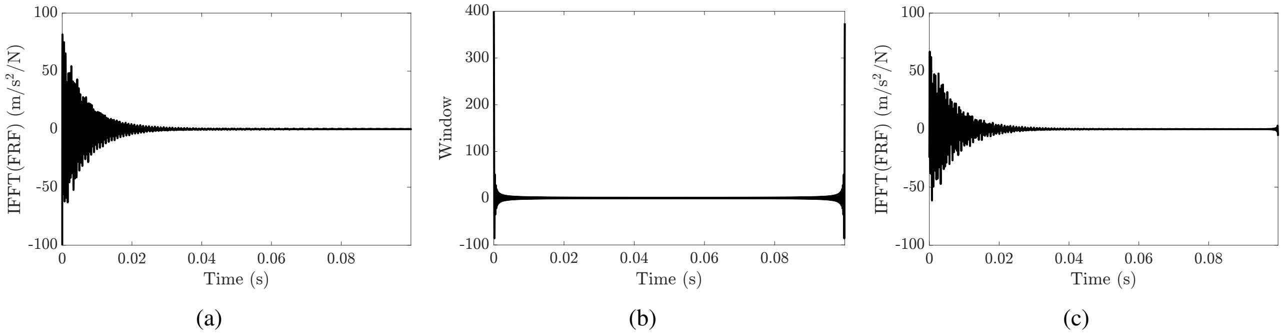

Fig. 2 Visualization of the effects of FRF frequency truncation on the estimated IRF. Subfigures are the IFFTs of the respective signals in Fig. 1. Subfigure (a) is convolved with (b) and downsampled to yield (c).

However, this bandpass artifact can be counterintuitive in light of the time-domain TWR formulation. Fig 3a shows an example of the tail of a band-limited IRF, and Fig. 3b shows the resulting input when the TWR problem is solved in a single-input, single-output configuration. The IRF tail results in input to the system before the first event in the spec, which will clearly generate a system repsponse. To visualize the analog case, the input, FRF, and specification are zero-padded in the frequency domain, which is equivalent to upsampling in the time domain. Figure 3c shows that, though the system responds before the first event in the spec, the output at the sampled time steps perfectly matches the specification. Hence, the early input to the system does not generate errors at the sampled time steps. The upsampled specification provides a reasonable visual of what the analog system output (or at least the analog specification) might look like, though it is not always intuitive. See Fig. 3d.

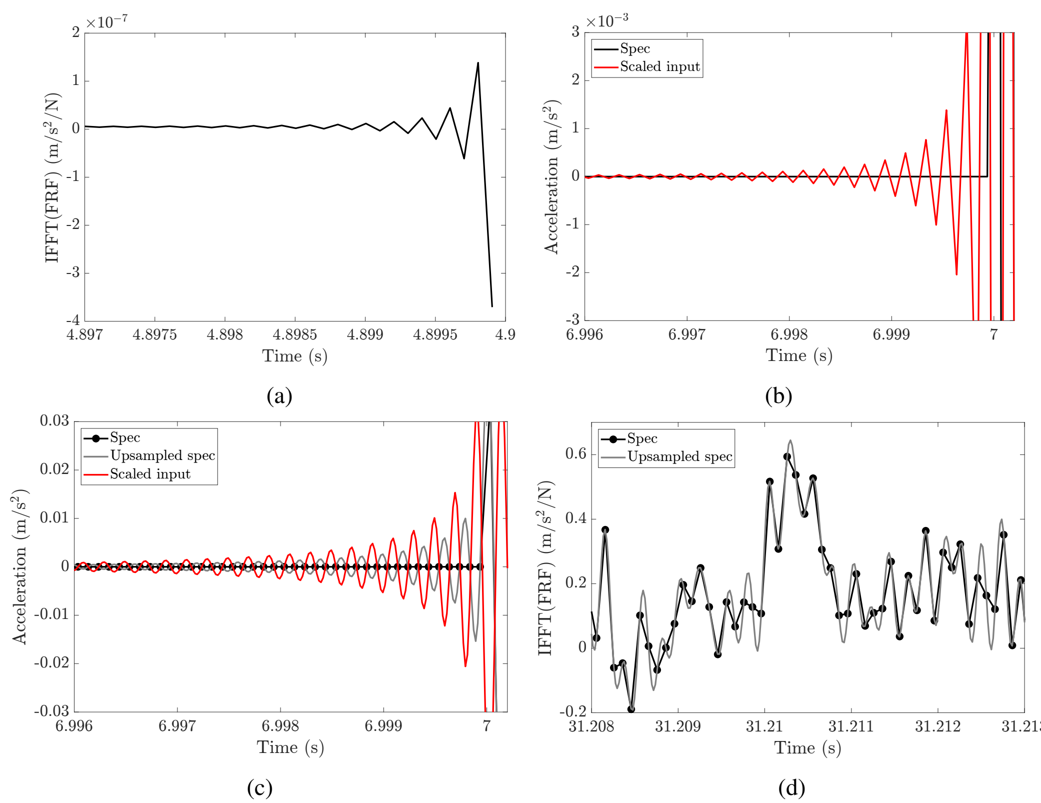

Fig. 3 Demonstration of the apparent non-causal inputs resulting from the application of a band-limited FRF to TWR. Subfigures show (a) the IFFT of a band-limited FRF (b) the first event in an ouptut specification overlayed with the solved input (c) the input, output, and specification after zero-padding in the frequency domain (d) an excerpt from the specification after zero-padding in the frequency domain.

The apparent non-causal IRF behavior caused by frequency truncation is, however, distinct from the artifacts caused by FRF measurement error. Fig. 4 shows the right tail of the IFFT of a discrete FRF with added Gaussian noise. Indeed, the tail has significant error, several orders of magnitude larger than the truncation effects in Fig. 3. The IRF errors are reflected by a large system input prior to the first event in the specification, when the system should not be responding. This error persists throughout the duration of the specification, often resulting in an audible echo that occurs in the output before events are prescribed by the specification.

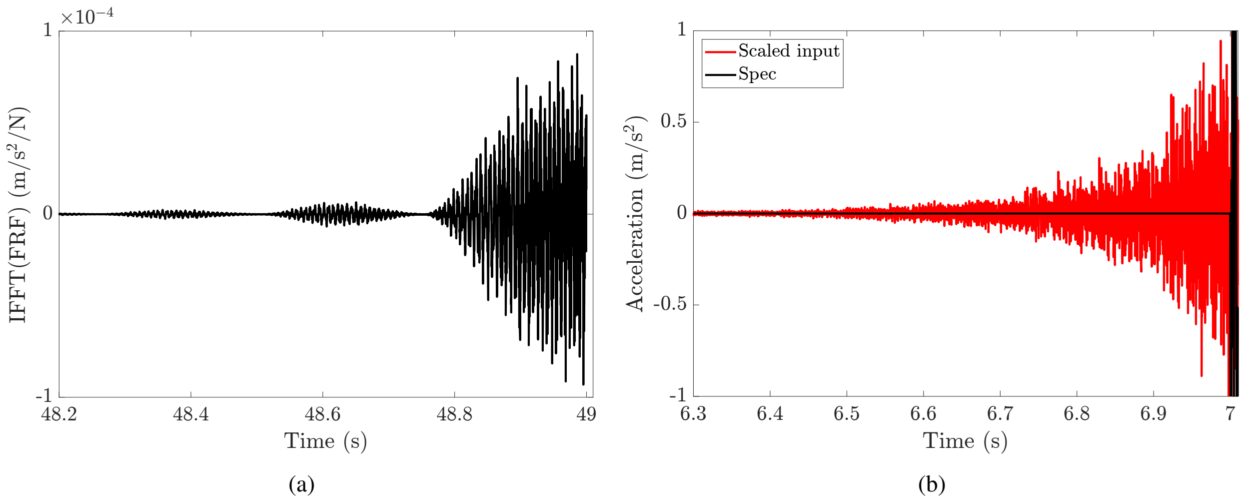

Fig. 4 Example of (a) an IFFT of a noisy, band-limited FRF and (b) the resulting non-causal system input (prior to the first event in the output specification) when that FRF is used in a TWR problem.

FRF Error Mitigation Methods

The frequency axis of $\widehat{\mathbf{H}}$ available from an experiment does not always match the frequency axis of the FFT of the specification. In the COLA framework, window sizes can be set to match the frequency resolution of the FRF. As an alternative, recent works [1, 12, 3] have proposed local modeling methods for FRF estimation. Local modeling methods rely on continuous FRF models, rather than discrete frequency bin averages, and any desired frequency axis can be specified in the FRF estimator. This work assumes that an FRF estimate has already been obtained with a frequency axis that does not necessarily match the specification. With the exception of the "minimum energy multilinear fit" method, frequency axis matching is performed in this paper using a standard complex linear interpolation. The modification methods are applied after interpolation.

Exponential taper (exp-taper) A simple, intuitive approach to correcting non-causal inputs that result from FRF noise is to remove the "ring-up" from the end of the IFFT of the FRF by multiplying it by an exponential window. Formally, the exponential taper used in this paper is

$$\widehat{\mathbf{H}}_{\text{exp-taper}}\left(\omega_k\right) = \mathcal{F}\left(\mathbf{H}\left(t_n\right) w\left(t_n\right)\right),$$
$$w\left(t_n\right) = \begin{cases} 1, & n \leq N - N_w \\ \exp\left[-\frac{5}{N_w\left(n+N_w-N+6\right)}\right], & n > N - N_w. \end{cases} \tag{3}$$

N_w is the number of points in the IFFT that are modified, and N is the total number of points. Though applying the exponential taper prevents the input signal from depending on future specification data (Fig. 4), it changes the system FRF, generating new errors. The effect of applying the exponential taper with $N_w = .05N$ is shown in the time and frequency domains in Fig. 5.

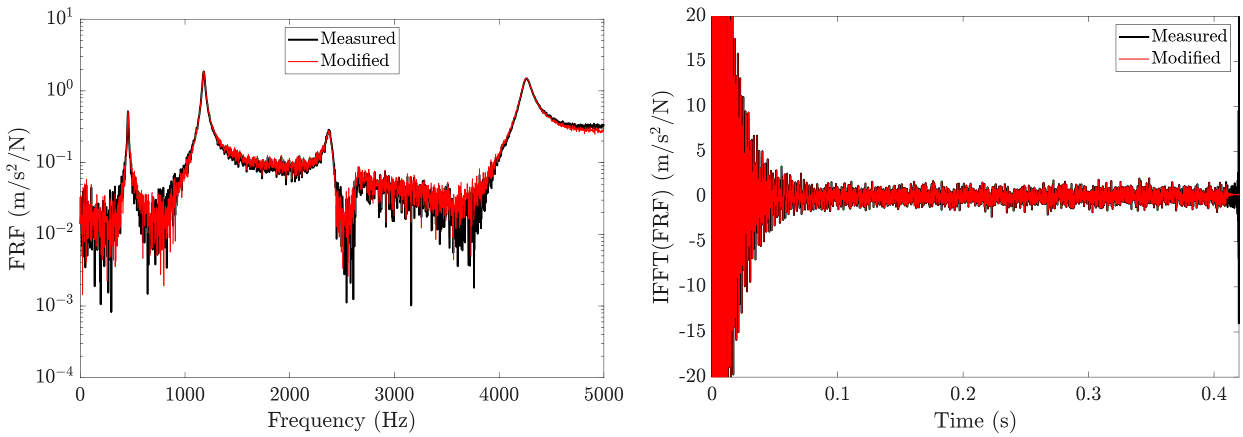

(a) (b)

Fig. 5 Effects of the exponential taper modification method on (a) a simulated FRF (b) the corresponding band-limited IRF.

Zero-pad, truncate (pad-trunc) The exponential taper removes the bandpass-filter end effects in the experimental IRF. Hence, applying a the exponential taper to a larger bandwidth FRF could reduce the effects, since a very high-frequency FRF should have negligible bandpass filter artifacts. The "pad-trunc" method is straightforward: zero-pad the FRF, apply the standard exponential taper (IFFT $\rightarrow$ taper $\rightarrow$ FFT), and truncate the FRF. If the alteration effects are largely confined to the higher (truncated frequencies), causality problems may be mitigated with a smaller effect on the bandwidth of interest. In this paper, the FRFs are zero-padded to ten times the original frequency band. An example of the pad-trunc modification method is shown in Fig. 6. A ring-up is still visible at the end of the IFFT, as desired, but the measured FRF is significantly altered in the bandwidth of interest, expecially around the anti-resonance at 3 kHz.

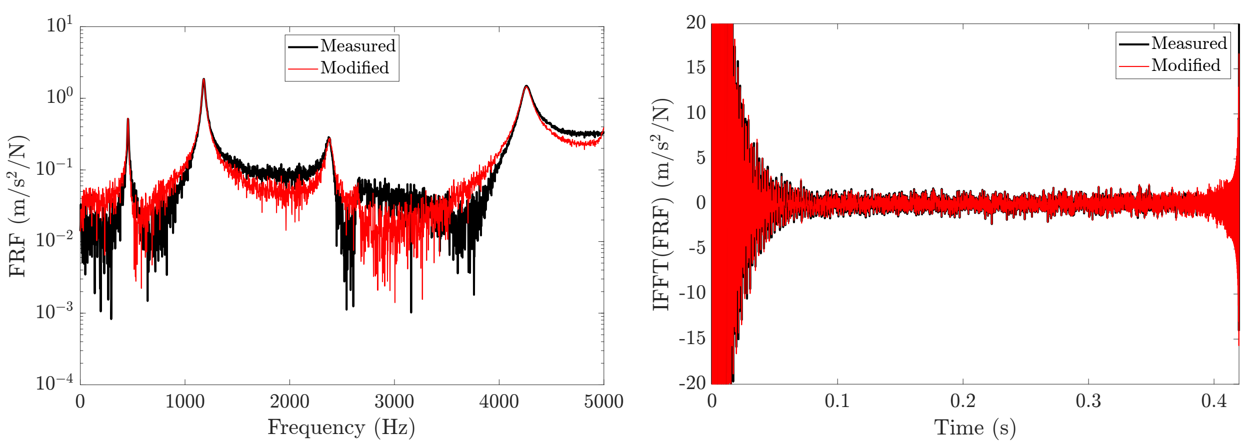

(a) (b)

Fig. 6 Effects of the zero pad, truncate modification method on (a) a simulated FRF (b) the corresponding band-limited IRF.

Optimal Hilbert causality enforcement (hilbert) In continuous linear systems, a causal system is defined as one whose impulse response function is zero for all $t < 0$. Let $\mathcal{H}$ denote the continuous hilbert transform operator. For an impulse response function $h(t)$, an equivalent definition of causality is $\mathcal{H}\left(h(t)\right) = -i\,h(t)$ [6]. The discrete Hilbert transform is a linear mapping, so applying the discrete version of the Hilbert transform identity is a simple linear constraint. Define $\mathbf{h}$ to be a vector containing the entries in the FRF $h\left(t_n\right)$ and let $\mathbf{A}\mathbf{h}$ contain the entries in $\mathcal{H}\left(h\left(t_n\right)\right)$, the discrete Hilbert transform.

Further, let $\mathbf{Bh} = \mathcal{F}(\mathbf{h})$. From a constrained optimization perspective, a reasonable objective is to compute

$$\begin{aligned} \min_{\mathbf{h}} \left(\mathbf{Bh} - \widehat{\mathbf{h}}_{\text{prior}}\right)^H \boldsymbol{\Sigma}^{-1} \left(\mathbf{Bh} - \widehat{\mathbf{h}}_{\text{prior}}\right) \\ \text{s.t.} \left(\mathbf{A} + i\mathbf{I}\right)\mathbf{h} = \mathbf{0}, \end{aligned} \tag{4}$$

where $\widehat{\mathbf{h}}_{\text{prior}}$ is the experimental FRF estimate. The constraint is always feasible, and a solution can be found by taking $\mathbf{h} = \mathbf{Nv}$, where $\mathbf{N}$ is the nullspace of $\mathbf{A} + i\mathbf{I}$. The optimimum is given by $\mathbf{N}^{+}(\boldsymbol{\Sigma})\,\widehat{\mathbf{x}}_{\text{prior}}$, where $\mathbf{N}^{+}(\boldsymbol{\Sigma})$ is the generalized pseudo-inverse. This method can be computationally prohibitive in large problems because $\mathbf{A}$ is $K \times K$. However, experience shows that if $\boldsymbol{\Sigma} = \mathbf{I}$, the Hilbert-optimal modification is very similar to setting $\mathbf{H}(t_n) = \mathbf{0}$ when $n = 0$ or $n \geq \lceil N/2 \rceil$. For the simulations in this paper, this form is used to compute the "hilbert" modification. Fig. 7 shows an example.

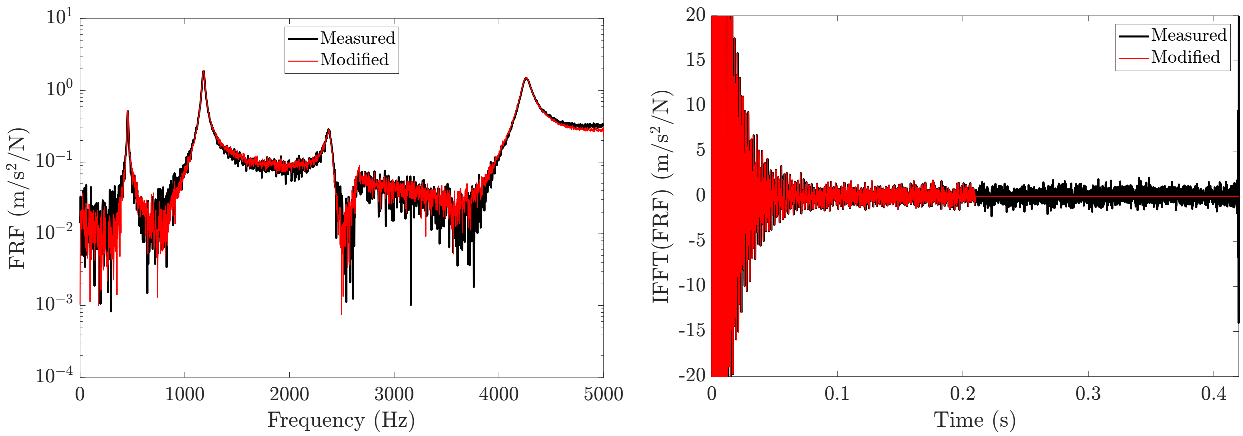

(a) (b)

Fig. 7 Effects of the Hilbert Transform contraint modification method on (a) a simulated FRF (b) the corresponding band-limited IRF.

Minimum energy multilinear fit (linear) Basis functions for FRF smoothing procedures are typically polynomial or rational functions. An alternative method, proposed herein, is to use single-mode FRFs as a basis for smoothing. Model j is given as a function of the frequency vector, $\boldsymbol{\omega}$, by

$$\mathbf{m}_j = \frac{1}{-\boldsymbol{\omega}^2 + 2i\zeta_j \boldsymbol{\omega}\omega_j + \omega_j^2}. \tag{5}$$

To reconstruct the de-noised FRF, $\mathbf{m}_j$ are assembled into the columns of $\mathbf{M}$, and weights of each linear model are selected according to

$$\min_{\mathbf{v}} \sigma_n \left(\mathbf{Mv} - \widehat{\mathbf{h}}_{\text{prior}}\right)^H \left(\mathbf{Mv} - \widehat{\mathbf{h}}_{\text{prior}}\right) + \frac{\sigma_v}{2}\mathbf{v}^T \boldsymbol{\Sigma}_v^{-1}\mathbf{v}. \tag{6}$$

Here σ_n and σ_v represent the energy of the noise and source vector, respectively. For a vibratory system, the weights of modal FRFs are determined by the mode shapes and should be strictly real, so the real and imaginary parts are separated to form a real problem,

$$\begin{aligned} &\min_{\mathbf{v}} \sigma_n \left(\overline{\mathbf{M}}\mathbf{v} - \overline{\mathbf{h}}\right)^T \left(\overline{\mathbf{M}}\mathbf{v} - \overline{\mathbf{h}}\right) + \sigma_v \mathbf{v}^T \boldsymbol{\Sigma}_v^{-1}\mathbf{v}, \\ &\overline{\mathbf{M}} = \begin{bmatrix} \text{Real}(\mathbf{M}) \\ -\text{Imag}(\mathbf{M}) \end{bmatrix}, \overline{\mathbf{h}} = \begin{bmatrix} \text{Real}\left(\widehat{\mathbf{h}}_{\text{prior}}\right) \\ \text{Imag}\left(\widehat{\mathbf{h}}_{\text{prior}}\right) \end{bmatrix}. \end{aligned} \tag{7}$$

This is a Tikhonov-regularized inverse solution to the least-squares problem $\mathbf{Mv} = \mathbf{x}$, and the selection of the parameters σ_n and σ_v is performed automatically using the procedure described in refs [13, 14]. Once the parameters are selected, the regularized inverse is given by

$$\hat{\mathbf{v}} = \left(\overline{\mathbf{M}}^T\overline{\mathbf{M}} + \frac{\sigma_n}{\sigma_v}\boldsymbol{\Sigma}_v^{-1}\right)^{-1} \overline{\mathbf{M}}^T\overline{\mathbf{h}}. \tag{8}$$

The covariance matrix, $\mathbf{\Sigma}_v$, represents the penalty on the size of each entry in $\mathbf{v}$. Setting $\mathbf{\Sigma}_v = \mathbf{I}$ risks overfitting, especially because low-frequency, lightly dampled modes have very narrow resonance peaks. If a sparse experimental FRF is curve-fit, low-frequency noise can result in large, lightly damped modes where measurement noise dominates. To ensure that the Tikhonov regularization works as desired and minimizing the energy of the curve fit, the magnitude of each curve $\mathbf{m}_j$ is squared and integrated over frequency to yield p_j, the power associated with curve j. The covariance is specified as a diagonal matrix with $\mathbf{\Sigma}_{v,jj} = p_j^{-1}$ so that the penalty term carries an equal weight for the contribution of each curve to the total energy of the fitted FRF.

Curve fitting is performed using a basis of 1200 single-degree-of-freedom FRFs with varying resonance frequencies and damping ratios.. Frequencies ω_j are set my multiplying the 40 most prominent peaks in the measured FRF by $\{0.99, 1.00, 1.01\}$ and combining every resulting frequency with modal dampings $\{0.005, 0.01, \ldots, 0.05\}$. The set of curves can be tailored to the particular application. This process is distinct from modal parameter selection: all of the curves are allowed to contribute to the smoothed FRF (even curves with overlapping frequencies), so the resulting FRF is composed of linear FRFs but is not a modal model. The results of the multilinear fit applied to the simulation in Fig. 9 are show in Fig. 8.

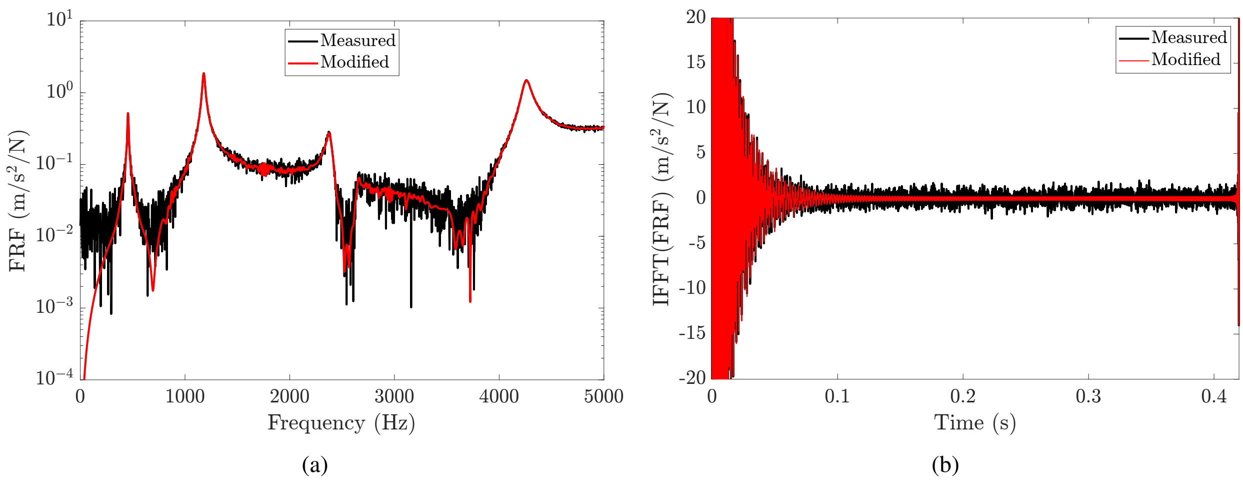

Fig. 8 Effects of the minimum-energy multilinear fit on (a) a simulated FRF (b) the corresponding band-limited IRF.

Simulation Results

The simulation is a simple linear spring-mass assembly with eight degrees of freedom (DOFs). Modal damping is set to 1% for all modes, and the FRF is truncated at 5 kHz as shown in Fig. 9b. Complex Gaussian noise is added at a specified signal-to-noise ratio. The specification is derived from an excerpt from a rock music song that is bandpass-filtered to a maximum frequency of 5 kHz and resampled at 10 kHz. The two-channel audio is distributed across the eight DOFs as shown in Fig. 9a.

Table 1 Masses and stiffnesses in the simulation structure.

	$j=1$	$j=2$	$j=3$	$j=4$	$j=5$	$j=6$	$j=7$	$j=8$
m_j (kg)	8	4	5.5	6	2	1	10	6
k_j (10^9 N/m)	2	1	2	4	2	0.5	5	1

Fig. 10 shows performance of the modification methods across a range of signal-to-noise ratios (SNRs). The error metric used is a normalized sum of squared errors,

$$\text{error} = \frac{\sum_n \left[\mathbf{y}(t_n) - \mathbf{y}_{\text{spec}}(t_n)\right]^2}{\sum_n \left[\mathbf{y}_{\text{spec}}(t_n)\right]^2}. \tag{9}$$

Each data point shows the mean of ten random trials with identical parameters. The linear fit method performs the best by a significant margin. However, in a simple linear simulation, this is not surprising, so the method should be receive

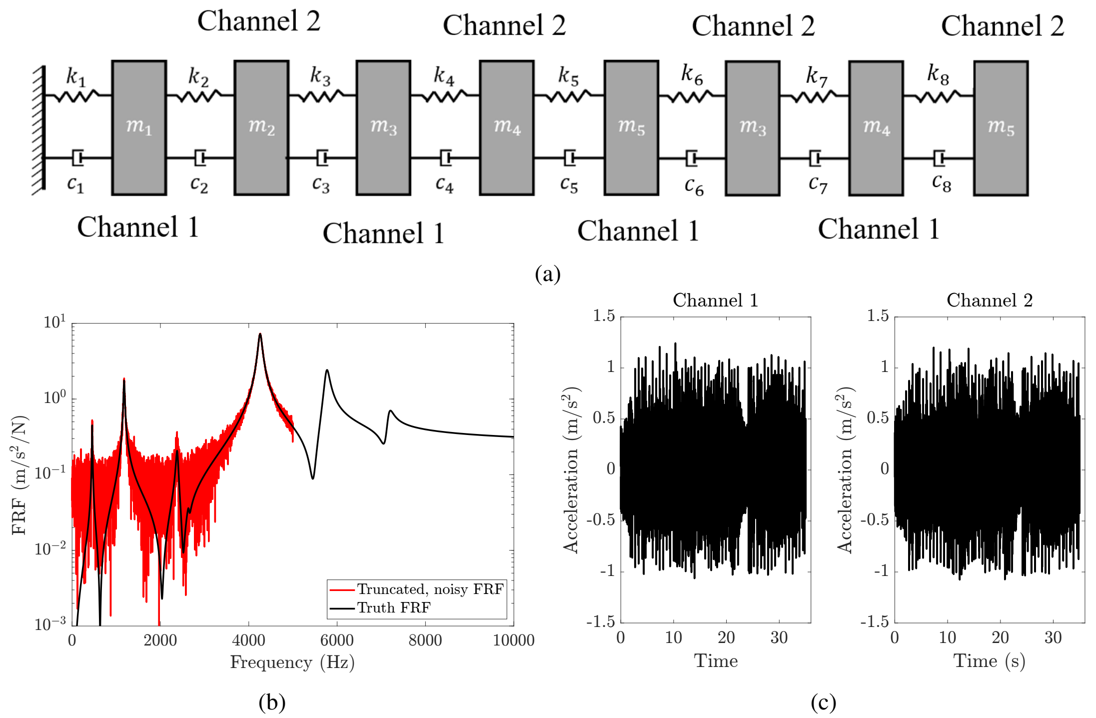

Fig. 9 Simulation case used for verification. Subfigures are (a) the simulation structure with values given in Table 1, (b) a noisy FRF (25 dB SNR), and (c) the two-channel output waveform specification.

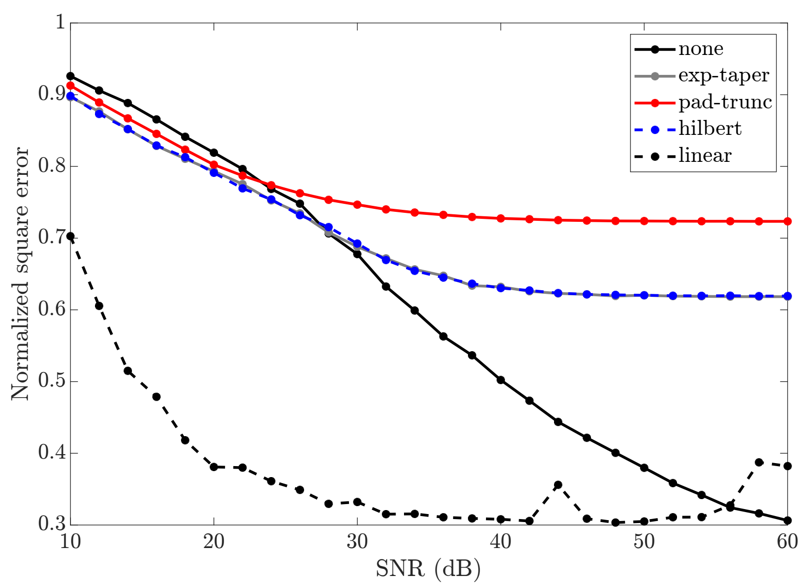

Fig. 10 Brief comparison of TWR performance for the four discussed FRF modification methods across a range of signal-to-noise ratios (SNRs).

further testing and validation. In low-noise scenarios (about 30 dB and higher SNR), applying the exponential taper or Hilbert transform modification increases error. That is, the bias generated by FRF modification exceeds the benefits of noise mitigation. In noisy scenarios, the exponential taper and Hilber modifications remove more error than they generate, yielding modest improvements in TWR.

Conclusion

This paper provides an overview of open-loop time waveform replication and describes problems associated with apparent non-causal impulse response functions. Errors in TWR are shown to result from FRF error and not from a frequency truncation in the measured FRF. In a window-free TWR framework, several FRF noise mitigation techniques are discussed and compared. In a MIMO simulation, simple FRF modifications are shown to improve TWR in very noisy cases, but they increase error in low-noise configurations. A minimum-energy multilinear FRF smoother reduces error significantly at most SNRs.

This paper provides a framework for TWR causality investigation, but many questions remain. Gaussian error was tested, and results may change if there are systematic FRF errors (such as those from leakage) or if the system is nonlinear. Further, theoretical analysis is needed to precisely determine when applying an FRF modification is benefitial and when it is detrimental. Finally, an experimental study should be performed, in particular to validate the "linear" method, which shows promise in a basic linear simulation.

Acknowledgments Sandia National Laboratories is a multi-mission laboratory managed and operated by National Technology & Engineering Solutions of Sandia, LLC (NTESS), a wholly owned subsidiary of Honeywell International Inc., for the U.S. Department of Energy's National Nuclear Security Administration (DOE/NNSA) under contract DE-NA0003525. This written work is authored by an employee of NTESS. The employee, not NTESS, owns the right, title and interest in and to the written work and is responsible for its contents. Any subjective views or opinions that might be expressed in the written work do not necessarily represent the views of the U.S. Government. The publisher acknowledges that the U.S. Government retains a non-exclusive, paid-up, irrevocable, world-wide license to publish or reproduce the published form of this written work or allow others to do so, for U.S. Government purposes. The DOE will provide public access to results of federally sponsored research in accordance with the DOE Public Access Plan.

References

1. Robbert Voorhoeve, Annemiek van der Maas, and Tom Oomen. Non-parametric identification of multivariable systems: A local rational modeling approach with application to a vibration isolation benchmark. *Mechanical Systems and Signal Processing*, 105:129–152, 2018.
2. Randall J. Allemang, Rohit S. Patwardhan, Murali M. Kolluri, and Allyn W. Phillips. Frequency response function estimation techniques and the corresponding coherence functions: A review and update. *Mechanical Systems and Signal Processing*, 162:108100, 2022.
3. Keaton Coletti, Ryan Schultz, and Steven Carter. A practitioner's guide to local FRF estimation. Technical Report SAND2023-07734C, Albuquerque, NM, February 2024.
4. Bram Cornelis, Alessandro Toso, Wouter Verpoest, and Bart Peeters. Improved MIMO FRF estimation and model updating for robust time waveform replication on durability test rigs. In *International Conference on Noise and Vibration Engineering*, Leuven, Belgium, September 2014.
5. Rodrigo A. Gonzalez, Patricio E. Valenzuela, Cristian R. Rojas, and Ricardo A. Rojas. Optimal enforcement of causality in non-parametric transfer function estimation. *IEEE Control Systems Letters*, 1(2):268–273, 2017.
6. P. Triverio and S. Grivet-Talocia. On checking causality of bandlimited sampled frequency responses. In *2006 Ph.D. Research in Microelectronics and Electronics*, Ontranto, Italy, June 2006. IEEE.
7. L. Faes, A. Porta, and G. Nollo. Testing frequency-domain causality in multivariate time series. *IEEE Transactions on Biomedical Engineering*, 57(8):1897–1906, 2010.
8. Jaeyong Cho, Karam Hwang, Seungil Jeung, and Seungyoung Ahn. An efficient extrapolation method of band-limited S-parameters for extracting causal impulse responses. *IEEE Transactions on Computer-Aided Design of Integrated Circuits and Systems*, 38(11):2086–2098, 2019.
9. Lyudmyla L. Barannyk, Hazem A. Aboutaleb, Aicha Elshabini, and Fred D. Barlow. Spectrally accurate causality enforcement using SVD-based Fourier continuations for high-speed digital interconnects. *IEEE Transactions on Components, Packaging and Manufacturing Technology*, 5(7):991–1005, 2015.
10. Jaeyong Cho, Jangyong Ahn, Jongwook Kim, Jaehyoung Park, Yujun Shin, Kibeom Kim, Junsung Choi, and Seungyoung Ahn. Low- and high-frequency extrapolation of band-limited frequency responses to extract delay causal time responses. *IEEE Transactions on Electromagnetic Compatibility*, 63(3):888–901, 2021.
11. W. G., William H. Press, Saul A. Teukolsky, William T. Vetterling, and Brian P. Flannery. *Numerical Recipes in Fortran 77: The Art of Scientific Computing.*, volume 1 of *Fortran Numerical Recipes*. Cambridge University Press, 1986.
12. Rik Pintelton, Dries Peumans, Gerd Vandersteen, and John Lataire. Frequency response function measurements via local rational modeling, revisited. *IEEE Transactions on Instrumentation and Measurement*, 70, 2021.
13. A. Pereira, J. Antoni, and Q. Leclère. Empirical Bayesian regularization of the inverse acoustic problem. *Applied Acoustics*, 97:11–29, 2015.
14. Garrett K. Lopp and Ryan Schultz. Bayesian-based response expansion and uncertainty quantification using sparse measurement sets. *Mechanical Systems and Signal Processing*, 169:107566, 2022.